CrossMark

Effects of the Growth Rate on Microstructures and Room Temperature Mechanical Properties of Directionally Solidified Mg-5.2Zn Alloy

SHAOJUN LIU,[1] GUANGYU YANG,[1,2] LEI XIAO,[1] SHIFENG LUO,[1] and WANQI JIE[1]

1.—State Key Laboratory of Solidification Processing, Northwestern Polytechnical University, No. 127 Youyi Western Road, Xi'an 710072, People's Republic of China. 2.—e-mail: ygy@nwpu.edu.cn

Effects of the growth rate on the microstructures and room temperature mechanical properties of Mg-5.2Zn alloy were investigated using Bridgman method at a constant temperature gradient 30 K/mm with different growth rates ($v = 10 \sim 100$ μm/s). The microstructure of directionally solidified Mg-5.2Zn alloy is composed of dendrite primary α(Mg) phase and interdendritic α(Mg) + Mg$_7$Zn$_3$ eutectic, which agrees well with the predicted microstructure using Scheil model. The morphology of the primary α(Mg) phase transforms from cellular, to cellular-dendritic, and then to dendritic with the increase of growth rate from 10 μm/s to 100 μm/s. According to the Kurz–Fisher model, the approximate criterion growth rate for cellular/dendrite transition is determined to be about 12.7 μm/s, which just lies in the experimental result interval. Using non-linear fitting analysis, λ_1 (the primary dendrite arm spacing) and λ_2 (secondary dendrite arm spacing) were found to be dependent on v (growth rate) in the form of $\lambda_1 = 8.6964 \times 10^{-6} v^{-0.23983}$, $\lambda_2 = 1.7703 \times 10^{-6} v^{-0.34161}$, which is in good agreement with the calculated values by the Trivedi model and Kattamis–Flemings model, respectively. Furthermore, tensile test shows that the directional solidified experimental Mg-5.2Zn alloy shows higher strength than the non-directional solidified alloy under the same cooling rate. The dendritic structure shows higher strength than the cellular structure due to the fact that brittle interdendrite eutectic was refined in dendritic structures.

INTRODUCTION

Magnesium alloy has attracted serious concern in aerospace, automotive and military industries due to its low density, high stiffness, high specific strength and excellent damping properties.[1] But its poor high temperature performance, in particular yield strength and creep resistance, is a challenge for its application at elevated temperature.[2] Alloying, e.g. adding rare earth elements into Mg-Zn alloys, is one of the possible choices to further improve the high temperature properties. Some promising Mg-Zn based alloys have been developed. For examples, Mg-3.5Zn-1.5Cu-0.6Gd (at.%) has been reported to have a high flow stress and a stable microstructure in the temperature range of 473–673 K[3] and thereby to have better creep resistance even compared with AE42 (Mg-4Al-2RE,

wt.%) alloy.[4] Mg-5.53Zn-1.08Y-0.73Zr (wt.%) alloy has a high ultimate tensile strength (230 MPa) and yield strength (163 MPa) in as-cast state.[5] The mechanical properties at room temperature and elevated temperature of Mg-4.58Zn-2.6Gd-0.18Zr (wt.%) sand cast alloy is much higher than that of ZK51A alloy (Mg-5.0Zn-0.6Zr, wt.%).[6] In addition, ZK60 (Mg-6Zn-0.6Zr, wt.%) alloy is widely used in both cast and wrought products due to its high yield strength of ~260 MPa, excellent damping capacity and high stability.[7] It is worthwhile to note that Zn concentration in these developed Mg-Zn based alloys varies within the range of 4–8 wt.%. It is, therefore, essential to elucidate the solidification behavior of Mg-rich alloys in Mg-Zn binary system under different casting conditions, especially under directional solidification condition.

Effects of the Growth Rate on Microstructures and Room Temperature Mechanical Properties
of Directionally Solidified Mg-5.2Zn Alloy

3215

Directional solidification technique has been reported to optimize the microstructure and to improve the mechanical properties.[8–11] Paliwal et al.[8] investigated the comprehensive microstructural evolution of Mg-3 wt.%, 6 wt.%, and 9 wt.% Al alloys by using directional solidification and other solidification techniques and built a solidification map based on the experimental data and the solidification model. Liu et al.[9] have studied the microstructure and mechanical properties of directionally solidified Mg-3.0Nd-1.5Gd alloy. A significant improvement of ultimate tensile strength (UTS) (59% higher) and elongation (112% higher) was obtained when comparing with the non-directionally solidified alloy under the same cooling rates. However, to date, only a few attempts[10,11] have been taken to elucidate this issue in Mg-Zn based alloys. Paliwal et al.[10] investigated the microstructure evolution of Mg-1.5, 4.0 and 5.5 Zn wt.% using directional solidification and wedge casting. Wang et al.[11] studied the dendritic growth orientations and three-dimensional morphologies of α(Mg) on Mg-40wt.% Zn alloy. There is still a lack of adequate understanding of the relations between solidification parameters and solidified microstructure as well as the mechanical properties of Mg-Zn based alloys.

In this paper, the microstructure and mechanical properties of directional solidified Mg-5.2Zn alloy under different growth parameters were investigated, with the aim to further explore solidification behaviors of Mg-Zn binary magnesium alloy. The effect of growth rates is also discussed on the basis of Kurz–Fisher model, Trivedi model and Kattamis–Flemings model, respectively.

THEORETICAL MODELS

Over the past decades, the relationship between the solidification processing parameters and dendrite spacing (the primary dendrite arms spacing λ_1 and secondary dendrite arms spacing λ_2) was established experimentally and theoretically.

Theoretical models have been proposed in the literature to describe λ_1 as a function of G, v and C_0 by Hunt,[12] Kurz and Fisher[13] and Trivedi.[14] Hunt attempted to allow for the interaction of the diffusion fields between neighboring cells. The relationship between solidification processing parameter and λ_1 for a dendritic front with the growth condition is determined by the minimum undercooling. The Hunt[12] model gives as,

$$\lambda_1 = 2.83[m(k-1)D\Gamma]^{0.25}C_0^{0.25}v^{-0.25}G^{-0.5} \quad (1)$$

Where, Γ is the Gibbs–Thomson coefficient, m is the liquilus slope, k is the distribution coefficient, C_0 is the initial composition of the solidifying alloy and D is the diffusion coefficient of solute atom in the liquid.

Kurz and Fisher[13] assumed that the shape of the dendrite fully developed, including side branches can be approximated as an ellipsoidal revolution and using the marginal stability criterion for an isolated dendrite. The Kurz and Fisher[13] model gives as follows,

$$\lambda_1 = 4.3[m(k-1)D\Gamma/k^2]^{0.25}C_0^{0.25}v^{-0.25}G^{-0.5} \quad (2)$$

The other theoretical model to characterize λ_1 as function of G, v, C_0 was developed by Trivedi.[14] Trivedi model is a result of the modification of the Hunt model, and used marginal stability criterion. Trivedi model gives,

$$\lambda_1 = 2.83[m(k-1)D\Gamma L]^{0.25}C_0^{0.25}v^{-0.25}G^{-0.5} \quad (3)$$

where, L is a constant that depends on harmonic perturbations. These theoretical models are very similar at high growth rate for λ_1 and the difference among them is only a constant.

For the secondary dendrite arms spacing λ_2, Langer and Müller-Krumbhaar[15] carried out a detailed numerical analysis of the wavelength of instabilities along the sides of a dendrite and predicted the scaling law as $\lambda_2/R = 2$. Using the scaling law $\lambda_2/R = 2$, the variation in λ_2 for small pelect number conditions given by Trivedi[16] was obtained as,

$$\lambda_2 = (8D\Gamma L/kV\Delta T_0)^{0.5} \quad (4)$$

where ΔT_0 is the difference between the liquidus and solidus equilibrium temperatures.

Bouchard and Kirkaldy[17] derived an expression, which is very similar to the marginal wavelength formula,

$$\lambda_2 = 2\pi a_2 \left(\frac{4\Gamma}{C_0(1-k)^2 T_F} \left(\frac{D}{v}\right)^2 \right)^{1/3} \quad (5)$$

where, a_2 is the secondary dendrite-calibrating factor, which depends on the alloy composition and T_F is the fusion teperature of the solvent.

Kattamis and Flemings[18] proposed a model to predict the secondary dendrite spacing based on a coarsening mechanism similar to the Ostwald ripening phenomenon in which the growth of a dendrite takes place by the dissolution od smaller dendrites in the melt. Kattamis and Flemings's model considered the cylinrical shaped (different radii) and two side branches (arms) of a growing columnar dendrite and assumed the presence of uniform temperature along the side branches. The proposed mathematical formulation by Kattamis and Flemings's model can be writted as,

$$\lambda_2 = 5.5 \left(-\frac{\Gamma D \ln\left(\frac{C_e}{C_0}\right)}{m(1-k)(C_e-C_0)t_f} \right)^{1/3} \quad (6)$$

where C_e is the eutectic composition and t_f is the solidification time.

EXPERIMENTAL PROCEDURE

Alloy Preparation

The experimental Mg-5.2 Zn (wt.%) alloy was prepared from pure Mg (99.98) and pure Zn (99.9), melt in an electrical-resistance furnace under the protection of anti-oxidizing flux (RJ4) and cast into an iron test bar at pouring temperature 720°C. The test bar was further processed into the samples of Φ 7.8 × 100 mm for directional solidification. The composition of the directionally solidification alloy was measured by inductively coupled plasma-optical emission spectrometry (ICP-OES).

Directional Solidification Experiments

A high temperature gradient Bridgman-type directional solidification furnace with a graphite heater and quenching system of water-cooled Ga-In-Sn liquid metals was used. The prepared sample (Φ 7.8 mm × 90 mm) was loaded in a special stainless steel crucible with 10 mm outer diameter, 8 mm inner diameter, 120 mm in length and sealed ends. The details of the experimental setup and procedure were described in Ref. 9 After the axial temperature gradient reaching 30 K/mm, the sample was directionally solidified by moving the crucible downward at a given speed (10–100 μm/s) for about 40 mm, and then quenched in Ga-In-Sn liquid metals. In this way, the withdrawal rate can be approximately evaluated to be the same as the growth rate.

Sample Characterization

The solidified samples were cut along both the longitudinal and transversal sections to investigate the quenched interface morphology and the solidification microstructure with Olympus PM-G3 type optical microscope (OM) and JEOL JSM-5800 type scanning electron microscope (SEM). The composition analysis of the second phases was conducted in an Oxford Inca type x-ray energy dispersive spectroscope (EDS). The x-ray diffraction (XRD) was performed on a X'Pert PRo MPD type instrument in the diffraction angle (2θ) ranging from 20° to 90°, using Cu Kα (λ = 0.154 nm) as a radiation source. The volume fraction of the second phase was measured by Image-Pro Plus 6.0 (Media Cybernetics, Inc., Bethesda, MD). The room temperature tensile properties were tested in a Zwick 150 type universal tensile testing machine with a maximum load of 150 KN and a strain rate of 1 mm/min. The samples for tensile tests are rectangular in the shape of 20 mm in length, 5 mm in width and 2 mm in height. At least three specimens were tested at each condition to ensure the reproducibility of the data.

RESULTS AND DISCUSSION

Directional Solidification Morphologies

As we all know, in directional solidification, solid/liquid interface morphology can be varied with growth rate, as shown in Fig. 1. The planar front will be exhibited when the growth rate is very slow. With increasing the growth rate up to v_c, the interface morphology will translated to cell structure. When the growth rate is close to v_{c-d}, the dendritic morphology is observed. Further increasing the growth rate, the cell structure and planar front will be occurred again.

Figure 2 shows longitudinal and transversal sections of OM microstructures of Mg-5.2Zn alloy quenched during directional solidification under the fixed temperature gradient (G = 30 K/mm) and different growth rate (v). Two types of interface morphology of the primary α(Mg) phase were observed. When $v \leq 10$ μm/s, α(Mg) exhibits a typical cellular structure with coarse trunks along the longitudinal section and regular cellular structure on transversal section, as shown in Fig. 2a–b. When v = 20 μm/s, α(Mg) presents a morphology with co-existence of cellular and dendrite structure, as shown in Fig. 2c–d, which means the cellular/dendrite transition is taking place. When the growth rate increases further up to 40 μm/s, α(Mg) presents dendrite morphology along longitudinal section and typical six petaloid morphology on transversal section, as shown in Fig. 2c–d. With further increase of
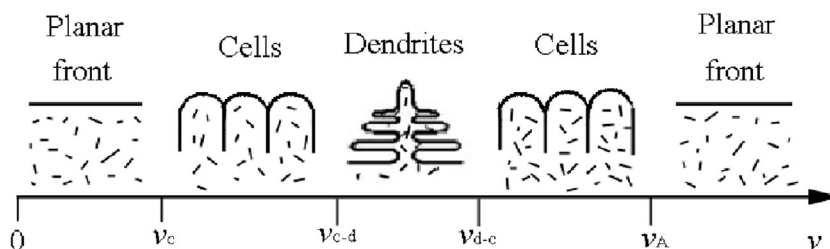

Fig. 1. Morphological diagram for solidification of binary systems illustrating the microstructural transitions "planar front" → "cellular structure" → "dendrites" → "cellular structure" → "planar front", with the increase in the solidification velocity v. Here v_c is the velocity given by the criterion of constitutional undercooling, v_{c-d} is the approximate criterion solidification velocity for cell/dendrite transition, v_{d-c} is the approximate criterion solidification velocity for dendrite/cell transition and v_A is the velocity for absolute morphological stability of the interface.
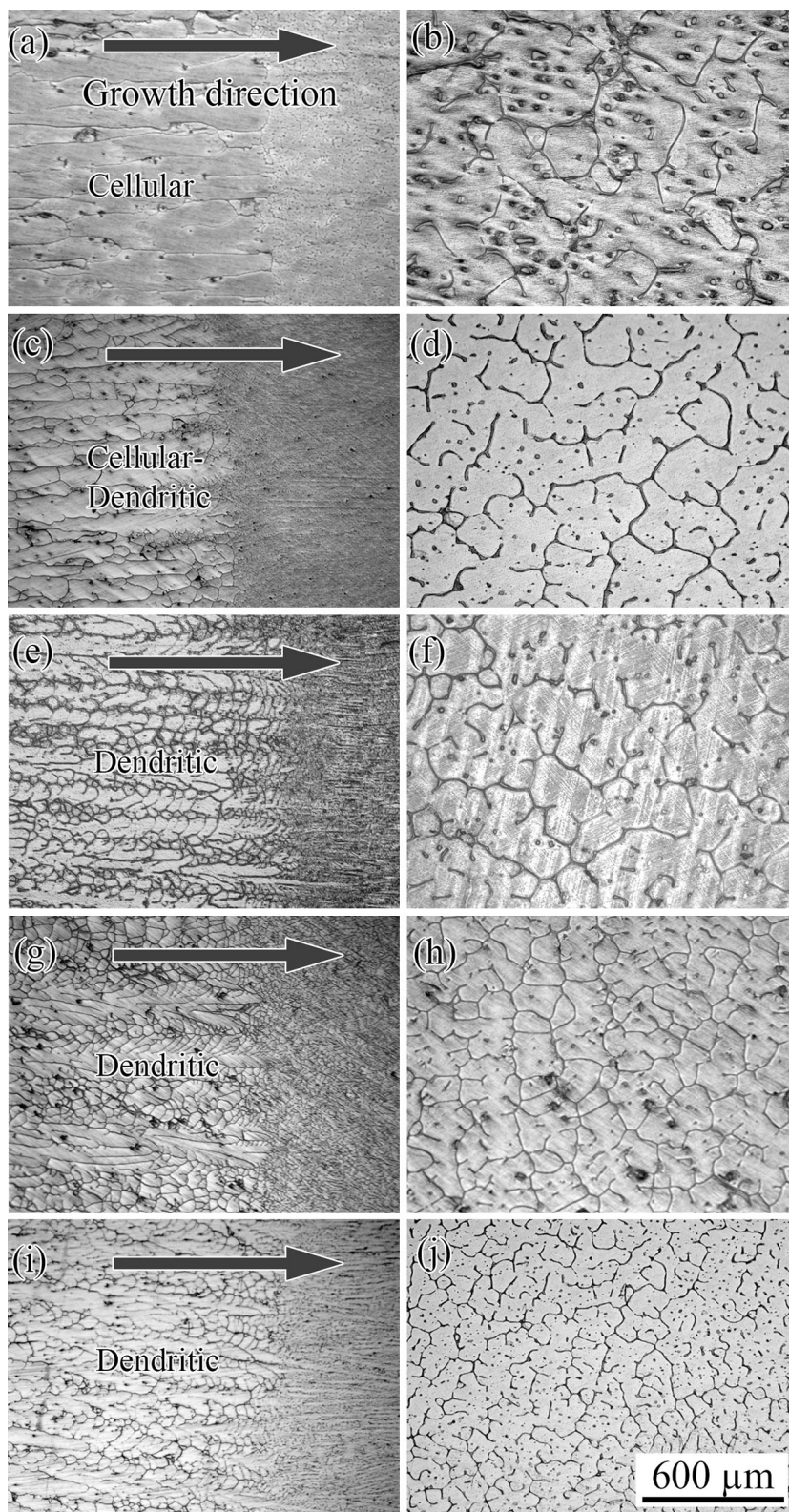
Fig. 2. OM microstructures of the directional solidified Mg-5.2Zn alloy under G = 30 K/mm at different growth rate. (a) and (b) 10 μm/s, (c) and (d) 20 μm/s, (e) and (f) 40 μm/s, (g) and (h) 60 μm/s, (i) and (j) 100 μm/s. (a), (c), (e), (g) and (j) were taken from longitudinal sections, (b), (d), (f), (h) and (j) were taken from transversal sections. The same scale bar was used in (j).

Table I. Thermophysical parameters of Mg-5.2Zn alloy

Property	Symbol	Unit	Value	Ref.
Initial composition	c_0	wt.%	5.2	
Slope of liquid line	m	K/wt.%	-3.102	[a]
Distribution coefficient	k_0	–	0.0804	[a]
Diffusion coefficient (liquid)	D	m^2/s	5.5×10^{-9}	[11]
Gibbs–Thomson coefficient	Γ	m K	1.1×10^{-7}	[11]

[a]The data is calculated using Thermo-Calc software.

growth rate, the primary dendrite arms (λ_1) and secondary dendrite arms (λ_2) become finer, as shown in Fig. 2e–j. It can be concluded that the critical growth rate of cellular/dendrite transition (v_{tr}) of the experimental alloy is between 10 μm/s and 40 μm/s under the temperature gradient of $G = 30$ K/mm.

The cellular/dendrite transition is one of the most fundamental and important solidification events during the directional solidification of alloys. Based on the dendrite growth theory of Kurz–Fisher,[19] the approximate criterion growth rate (v_{tr}) for cellular/dendrite transition can be expressed as,

$$v_{tr} = \frac{GD}{\Delta T_0 k} = \frac{GD}{mC_0(k-1)} \quad (7)$$

where, G is the temperature gradient in the liquid, D is the diffusion coefficient of solute atom in the liquid, ΔT_0 is the temperature interval between the liquidus and the solidus, k is the solute partition coefficient, m is the slope of the liquidus and C_0 is the initial composition. Using the thermophysical parameters given in Table I, v_{tr} for Mg-5.2Zn alloy can be determined to be 12.7 μm/s, which just lies in the experimental result interval. It is noticed that the cellular/dendrite transition occurs in a wide range of the growth rates,[20] that's why α(Mg) presents a cellular-dendrite mixture morphology under the growth rate of 20 μm/s.

Interdendritic Phases

Figure 3a shows the equilibrium phase diagram of Mg-Zn binary system calculated from the thermodynamic description obtained by Agarwal et al.[21] using Thermo-Calc software.[22] The real chemical composition of Mg-5.2Zn alloy is marked by the dotted line in Fig. 3a. In the equilibrium condition, only α(Mg) phase will be formed during solidification. Using the Scheil simulation, based on the assumption of complete mixing the liquid but no diffusion in the solid, the solidification path of Mg-5.2Zn alloy was predicted as, Liquid $\rightarrow$ Liquid + α(Mg) $\rightarrow$ Liquid + α(Mg) + Mg$_7$Zn$_3$ $\rightarrow$ α(Mg) + Mg$_7$Zn$_3$, as shown in Fig. 3b. The primary phase is α(Mg), and the eutectic structure of α(Mg) + Mg$_7$Zn$_3$ forms at the late stage of solidification.

Figure 4 shows SEM microstructures of transversal section of the directional solidified tested alloy at the growth rate of 10 μm/s and 100 μm/s, respectively. The dark phase is identified to be α(Mg). Semi-continuous white phases are found along α(Mg) grain boundary and some dot-like white phases also presented within α(Mg) grain. From the local enlarger SEM images (Fig. 4c and d), the interdendritic white phase is indexed as α(Mg) + Mg$_7$Zn$_3$ eutectic phase according to the EDS patterns and XRD pattern, as shown in Figs. 4e–f and 5. Compared with the calculation results shown in Fig. 3b, it is concluded that the solidification microstructure is consistent with the prediction using Scheil model, which is believed to be close to the real solidification process.

The volume fractions of the second phases appear to decrease with increasing growth rates, as shown in Table II, due to the fact that a higher growth rate corresponds to a higher cooling rate, and leads to a reduced diffusion time for the eutectic phase growth.[2] The volume fraction of the second phase was also evaluated using Scheil model, as listed in Table II. Comparing with the image analysis results, the measured values are slightly less than the calculated value (7.975%) by Scheil model, which can be attributed to the fact that back diffusion of alloying elements is not taken into consideration in Scheil model but it occurs during the real solidification process.

Dendritic Microstructure Parameters

λ_1 and λ_2 are the main characteristic lengths, which are believed to have a significant effect on the mechanical properties such as yield strength and creep resistance of the alloy. The measured λ_1 and λ_2 are plotted in Fig. 6. As expected, λ_1 and λ_2 decreases with increasing v. From Fig. 6, it can be seen that the data form straight lines on the logarithmic scale. The linear regression analysis gives the proportionality equation as,[23]

$$\lambda = av^{b} \quad (8)$$

where a and b are constant, dependent on the alloy composition, temperature gradient and diffusion coefficient.

Effects of the Growth Rate on Microstructures and Room Temperature Mechanical Properties
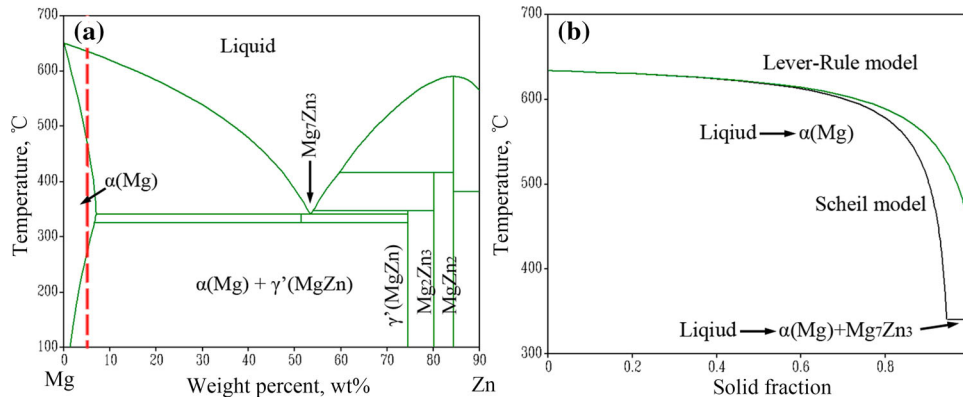of Directionally Solidified Mg-5.2Zn Alloy

3219

Fig. 3. Prediction of solidification process of Mg-Zn alloy with Thermo-Calc. (a) Equilibrium phase diagram of Mg-5.2Zn alloy, (b) solidification path of Mg-5.2Zn alloy.
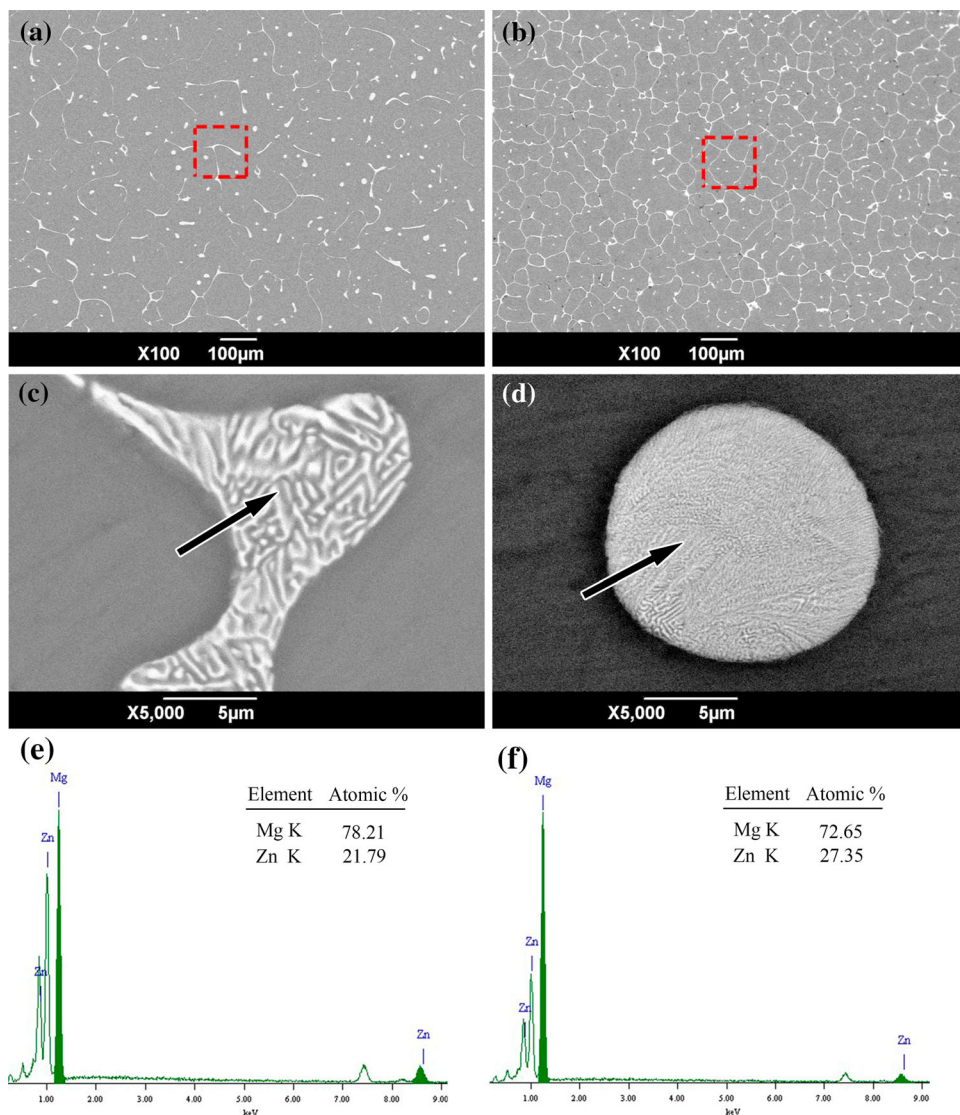

Fig. 4. SEM images of the directionally solidified Mg-5.2Zn alloy at the growth rate of 10 μm/s (a) and 100 μm/s (b). (a) and (b) were taken from transversal sections. (c) and (d) are enlarger from the local regions marked by dash lines in (a) and (b), respectively. (e) and (f) are the corresponding EDS patterns of interdendritic white phase, respectively.

Through non-linear regression analysis, λ_1 and λ_2 under the fixed G (30 K/mm) at the varied growth rates can be described as,

$$\lambda_1 = 8.6964 \times 10^{-6} v^{-0.23983} \quad (9)$$

$$\lambda_2 = 1.7703 \times 10^{-6} v^{-0.34161} \quad (10)$$

For the sake of comparison, the calculated λ_1 and λ_2 by different theoretical models are also given in Fig. 6. It can be seen from Fig. 6a that the calculated λ_1 with Trivedi model[14] show reasonable agreement with the experimental values. However, the calculated λ_1 with Hunt model[12] and Kurz–Fisher model[13] deviate significantly from the experimental results. From Fig. 6b, the calculated λ_2 by Kattamis–Flemings model[18] show reasonable agreement with the experimental values, this is mainly due to the fact that Kattamis–Flemings model developed based on coarsening mechanism similar to the Ostwald ripening phenomenon, which occurred in reality for the secondary arm.
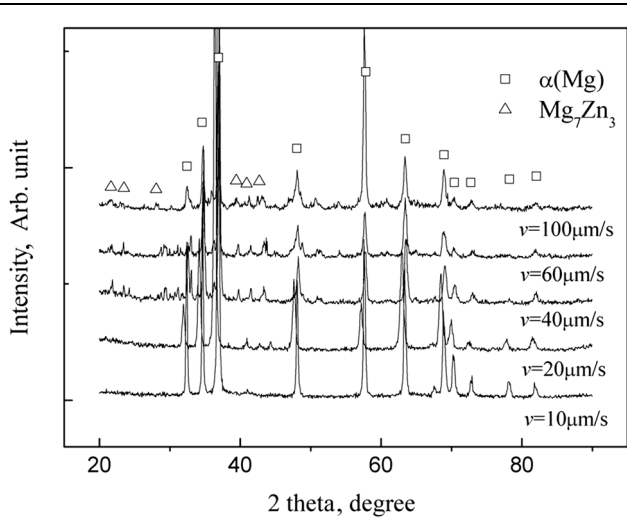
Room Temperature Mechanical Properties

Figure 7 shows the nominal stress versus nominal strain curves of the directionally solidified and non-directionally solidified Mg-5.2Zn alloy under the same cooling rate. The cooling rate of Mg-5.2Zn alloy cast in metallic mold was measured to be about 1.8 K/s, which is close to that of the directionally solidified experimental alloy under $G = 30$ K/mm and $v = 60$ μm/s. As can be seen from Fig. 7, the ultimate tensile strength and elongation were 186.3 MPa and 21.3% for the directionally solidified alloy and 160 MPa and 18.4% for the non-directionally solidified alloy.

Figure 8 shows the room temperature mechanical properties of the as-cast experimental alloys after directional solidification under different growth rates at $G = 30$ K/mm. For clarity, the corresponding microstructures are also indexed. It is found that when v increases from 10 μm/s, 20 μm/s to 40 μm/s, the ultimate tensile strength is improved from 128 MPa, 157 MPa to 181 MPa, and the corresponding primary α(Mg) phase exhibits cellular, cellular-dendritic and dendritic structure, respectively. Clearly, the ultimate tensile strength of Mg-5.2Zn alloy with dendritic morphology is stronger than the cellular one. After the cellular to dendritic transition, the ultimate tensile strength increases with further increasing of the growth rates.

In order to elucidate the differences of fracture behaviors between the cellular and dendritic forms, the fractures of Mg-5.2Zn alloys with cellular and dendritic morphologies were studied. Figure 9 shows SEM fracture surface images of the tested alloys with cellular and dendritic α(Mg) grains after the tensile test. The tested alloy with cellular structure shows islands of dimples separated by large cracks. The initiation and propagation of these cracks are responsible for its poor properties for the cellular structure alloy. By contrast, the tested alloy with dendritic structure exhibits a uniform surface consisting of fine dimples, which are evidence of totally ductile failure. Figure 10 shows OM fracture morphologies on longitudinal section of tensile samples with the cellular and dendritic structures, respectively. The sample with the cellular structure

Fig. 5. XRD patterns of the directional solidified Mg-5.2Zn alloys.

Table II. Volume fractions of the second phase in Mg-5.2Zn alloys

Temperature gradient G, K/mm	Growth rate v, μm/s	Cooling rate $R(R = Gv)$, K/s	Eutectic volume fraction/%	
			Image analysis results	Calculation results by Scheil model
30	10	0.3	7.89 (±0.3)	7.975
30	20	0.6	7.86 (±0.5)	7.975
30	40	1.2	7.33 (±0.5)	7.975
30	60	1.8	6.52 (±0.4)	7.975
30	100	3.0	6.11 (±0.5)	7.975

Effects of the Growth Rate on Microstructures and Room Temperature Mechanical Properties
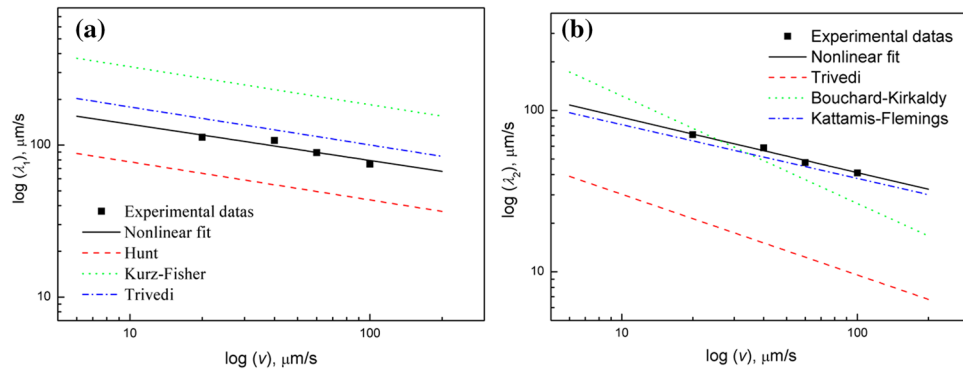of Directionally Solidified Mg-5.2Zn Alloy

3221

Fig. 6. Comparison of the observed dendritic spacing (λ_1, λ_2) with the calculated ones using different theory models. (a) the primary dendritic arm spacing (λ_1), (b) the secondary dendritic arm spacing (λ_2).
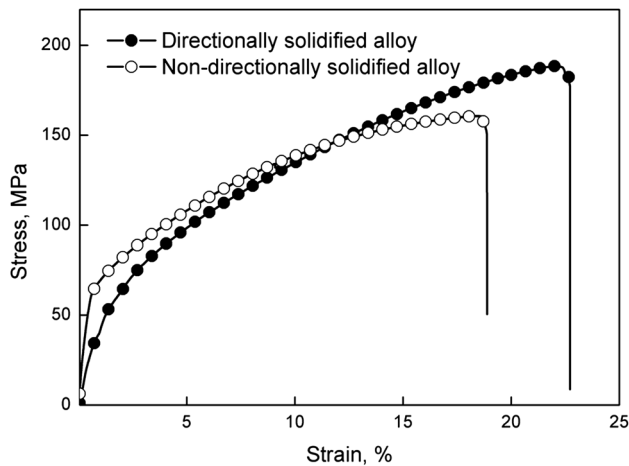

Fig. 7. The stress-strain curves for the directionally solidified and non-directionally solidified Mg-5.2Zn alloy under the same cooling rate.
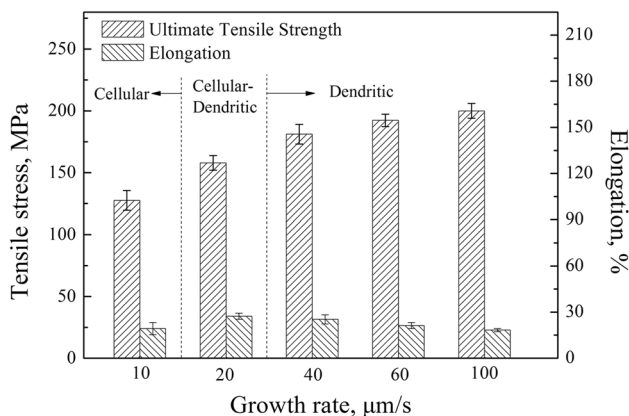

Fig. 8. Room temperature mechanical properties of the directionally solidified Mg-5.2Zn alloy under different growth rates at a constant G of 30 K/mm.

shows an intergranular failure, as shown in Fig. 10-a. In addition, large particles of interdendritic phase and continuous grain boundary films are also observed, which are prone to fracture under local stress concentration during tensile test. In the sample with the dendritic structure, extensive transgranular failure is observed, as shown in Fig. 10b.

Strengthening Mechanism

Apparently, as shown in Fig. 7, the directional solidification technology significantly improves the room temperature mechanical properties. This is mainly attributed to the fact[9] that directional solidification technology achieved sequence solidification in whole casting process, promoted α(Mg) grains formed parallel to the pulling direction and reduced the formation of solidification defects, such as shrinkage porosity and shrinkage cavity.

Furthermore, the different solidification morphology leads to different mechanical properties, as shown in Fig. 8, the ultimate strength tensile increases as the solidification morphology varied from cellular to cellular-dendritic and dendritic structure. During the solidification process with cellular growth interface, the interface consists of families of finger-like projections moving in unison while sweeping ahead the solute-rich liquid. The liquid at the interface contains a high concentration of solute elements, and it solidified, forming coarse brittle phases along the cellular boundaries, which serve as regions for crack initiation or propagation during the tensile test. By contrast, during solidification of the dendritic interface, the solute-rich liquid is entrained in the interdendritic spaces and separated by closely-spaced secondary and tertiary dendrite arms, then solidified with small size in isolated pockets, which could act as a reinforce phase to obstacle the dislocation slip and to prevent the grain deformation during the tensile test.[24] In addition, due to the refinement of the second phase in the dendrite form alloy makes it difficult for micro-cracks to initiate and propagate and thereby makes it more ductile compared with the case in the cellular form.
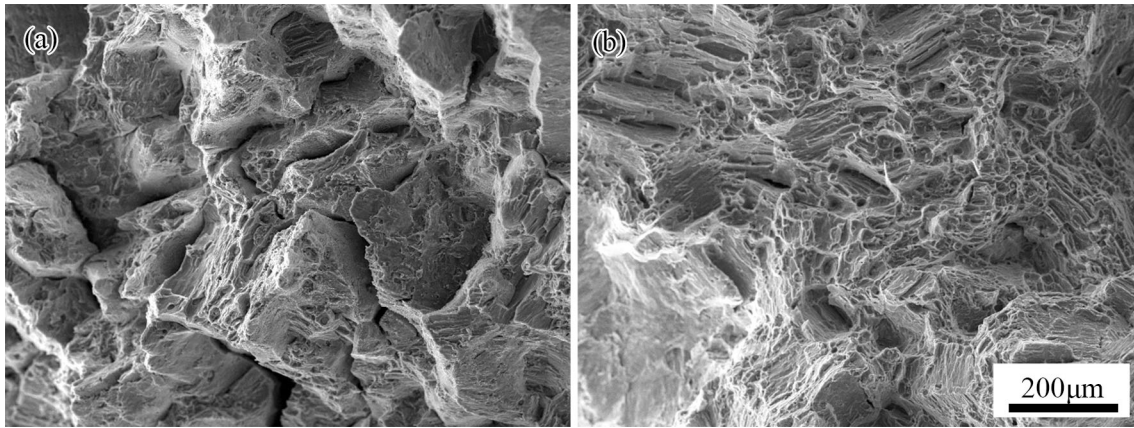
Fig. 9. SEM fracture morphologies of transversal section through room temperature fracture surface. (a) cellular structure (v = 10 μm/s), (b) dendritic structure (v = 40 μm/s).
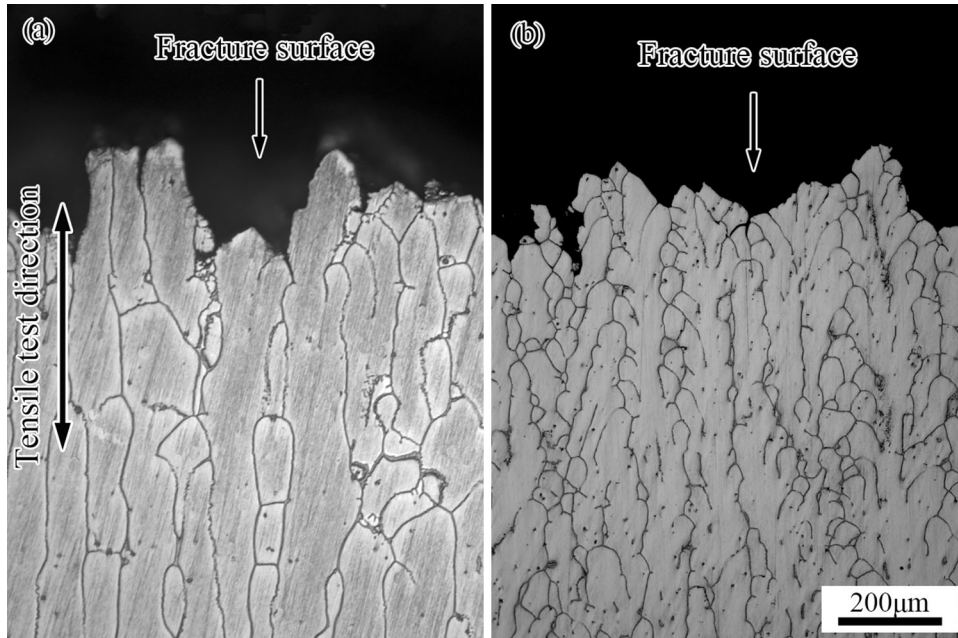

Fig. 10. OM fracture morphologies of longitudinal section after room temperature tensile test. (a) cellular structure (v = 10 μm/s), (b) dendritic structure (v = 40 μm/s).

CONCLUSION

Effects of the growth rate on microstructure and mechanical properties of directionally solidified Mg-5.2Zn binary alloy were investigated using Bridgman method. The main conclusions can be drawn as follows,

1) The microstructure of the directionally solidified Mg-5.2Zn alloy exhibits a transition from cellular, to cellular-dendritic, and then to dendritic growth, when the growth rate is increased from 10 μm/s to 40 μm/s. According to Kurz–Fisher model, the approximate criterion growth rate for cellular/dendrite transition is calculated to be 12.7 μm/s, which is in good agreement with the experimental results.

2) The primary dendrite arm spacing (λ_1) and the secondary dendrite arm spacing (λ_2) are dependent on the growth rate (v) in the form of $\lambda_1 = 8.6964 \times 10^{-6} \ v^{-0.23983}$, $\lambda_2 = 1.7703 \times 10^{-6} \ v^{-0.34161}$, which is in good agreement with the calculated values by the Trivedi model and Kattamis–Flemings model, respectively.

3) The directionally solidified Mg-5.2Zn alloy was mainly consisted of α(Mg) dendrite and interdendritic α(Mg) + Mg$_7$Zn$_3$ binary eutectic phases, as predicted microstructure using Scheil model.

4) The directionally solidified experimental Mg-5.2Zn alloy exhibits a higher strength than the

Effects of the Growth Rate on Microstructures and Room Temperature Mechanical Properties
of Directionally Solidified Mg-5.2Zn Alloy

3223

non-directionally solidified alloy. Meanwhile, the sample with dendritic α(Mg) is stronger than that in cellular form due to the fact that the formation tendency for brittle and coarse phase in the dendritic form is less than that in the cellular form.

REFERENCES

1. D. Sarker, J. Friedman, and D.L. Chen, *J. Mater. Sci. Technol.* 30, 884 (2014).
2. Z.W. Cai, F.X. Chen, and J.Q. Guo, *J. Alloy. Compd.* 648, 215 (2015).
3. Y. Liu, G.Y. Yuan, W.J. Ding, and C. Lu, *J. Alloy. Compd.* 427, 160 (2007).
4. G.Y. Yuan, H.M. Kato, and K.J. Amiya, *J. Mater. Res.* 20, 1278 (2005).
5. D.K. Xu, W.N. Tang, L. Liu, Y.B. Xu, and E.H. Han, *J. Alloy. Compd.* 432, 129 (2007).
6. S.J. Liu, G.Y. Yang, S.F. Luo, and W.Q. Jie, *J. Alloy. Compd.* 644, 846 (2015).
7. T. Bhattacharjee, C.L. Mendis, T.T. Sasaki, T. Ohkubo, and K. Hono, *Scripta Mater.* 67, 967 (2012).
8. M. Paliwal and I. Jung, *Acta Mater.* 61, 4848 (2013).
9. S.J. Liu, G.Y. Yang, and W.Q. Jie, *Acta Metall. Sin. (Engl. Lett.)* 27, 1134 (2014).
10. M. Paliwal and I. Jung, *J. Cryst. Growth* 394, 28 (2014).
11. M.Y. Wang, Y.J. Xu, T. Jing, G.Y. Peng, Y.N. Fu, and N. Chawla, *Scripta Mater.* 67, 629 (2012).
12. J.D. Hunt, *Solidification and Casting of Metals* (London: The Metal Society, 1979), p. 3.
13. W. Kurz and D.J. Fisher, *Acta Metall.* 29, 11 (1981).
14. R. Trivedi, *Metall. Trans. A* 15, 977 (1984).
15. J.S. Langer and H. Müller-Krumbhaar, *Acta Metall.* 26, 1681 (1978).
16. R. Trivedi and K. Somboonsuk, *Mater. Sci. Eng.* 65, 65 (1984).
17. D. Bouchard and J.S. Kirkaldy, *Metall. Mater. Trans. B* 28, 651 (1997).
18. T.Z. Kattamis and M.C. Flemings, *Trans. Met. Soc. AIME.* 28, 997 (1965).
19. M. Qu, L. Liu, Y. Cui, and F.B. Liu, *Trans. Nonferrous Met. Soc. China* 25, 405 (2015).
20. O.L. Rocha and C.A. Siqueira, *Mater. Sci. Eng., A* 347, 59 (2003).
21. R. Agarwal, S.G. Fries, H.L. Lukas, G. Petzow, F. Sommer, T.G. Chart, and G. Effenberg, *Z. Metallkd.* 83, 216 (1992).
22. J.O. Andersson, T. Helander, L. Höglund, P.F. Shi, and B. Sundman, *Calphad* 26, 273 (2002).
23. X.W. Hu, S.M. Li, W.J. Chen, S.F. Gao, L. Lin, and H.Z. Fu, *J. Alloy. Compd.* 484, 631 (2009).
24. J. Hofweber and N.F. Fiore, *Mater. Sci. Eng.* 27, 157 (1977).